

## CHARACTERISATION OF THE PARTICLE-INDUCED BACKGROUND OF XMM-NEWTON EPIC-PN: SHORT AND LONG TERM VARIABILITY

ESRA BULBUL,<sup>1</sup> RALPH KRAFT,<sup>1</sup> PAUL NULSEN,<sup>1,2</sup> MICHAEL FREYBERG,<sup>3</sup> ERIC D. MILLER,<sup>4</sup> CATHERINE GRANT,<sup>4</sup>  
MARK W. BAUTZ,<sup>4</sup> DAVID N. BURROWS,<sup>5</sup> STEVEN ALLEN,<sup>6</sup> TANJA ERAERDS,<sup>3</sup> VALENTINA FIORETTI,<sup>7</sup>  
FABIO GASTALDELLO,<sup>8</sup> VITTORIO GHIRARDINI,<sup>1</sup> DAVID HALL,<sup>9</sup> NORBERT MEIDINGER,<sup>3</sup> SILVANO MOLENDI,<sup>8</sup> ARNE RAU,<sup>3</sup>  
DAN WILKINS,<sup>6</sup> AND JOERN WILMS<sup>10</sup>

<sup>1</sup>*Center for Astrophysics | Harvard & Smithsonian, 60 Garden Street, Cambridge, MA 02138*

<sup>2</sup>*ICRAR, University of Western Australia, 35 Stirling Hwy, Crawley, WA 6009, Australia*

<sup>3</sup>*Max Planck Institute for Extraterrestrial Physics, Giessenbachstr. 1 85748, Garching, Germany*

<sup>4</sup>*Kavli Institute for Astrophysics and Space Research, Massachusetts Institute of Technology, 77 Massachusetts Avenue, Cambridge, MA 02139*

<sup>5</sup>*Pennsylvania State University, Department of Astronomy and Astrophysics, 525 Davey Lab, University Park, Pennsylvania 16802, USA*

<sup>6</sup>*Department of Physics, Stanford University, 382 Via Pueblo Mall, Stanford, CA 94305-4060, USA*

<sup>7</sup>*INAF Osservatorio di Astrofisica e Scienza dello Spazio di Bologna, via Gobetti 93/3, 40129 Bologna, Italy*

<sup>8</sup>*INAF/IASF-Milano, Via Bassini 15, 20133 Milano, Italy*

<sup>9</sup>*Centre for Electronic Imaging, The Open University, Walton Hall, Milton Keynes, MK7 6AA, UK*

<sup>10</sup>*Dr. Remeis-Sternwarte and Erlangen Centre for Astroparticle Physics, Universität Erlangen-Nürnberg, Sternwartstr. 7, 96049 Bamberg, Germany*

### ABSTRACT

The particle-induced background of X-ray observatories is produced by Galactic Cosmic Ray (GCR) primary protons, electrons, and He ions. Events due to direct interaction with the detector are usually removed by on board processing. The interactions of these primary particles with the detector environment produce secondary particles that mimic X-ray events from celestial sources and are much more difficult to identify. The filter wheel closed data from the *XMM-Newton* EPIC-pn camera in small window mode (SWM) contains both the X-ray-like background events and the events due to direct interactions with the primary particles. From this data we demonstrate that X-ray-like background events are spatially correlated with the primary particle interaction. This result can be used to further characterise and reduce the non-X-ray background in silicon-based X-ray detectors in current and future missions. We also show that spectrum and pattern fractions of secondary particle events are different from those produced by cosmic X-rays.

### 1. INTRODUCTION

X-ray studies of the assembly processes of extended large scale structures, constraints on cosmology and the nature of dark matter, and studies of the cosmic X-ray background that holds clues about the formation of the first black holes are among the primary science goals of current (e.g., *Chandra*, *XMM-Newton*, and SRG) and future X-ray telescopes (*Athena*, *Lynx*) (Nandra et al. 2013; Gaskin et al. 2019). These measurements are sensitive to the level of the total flux and related system-

atic uncertainties of the instrumental X-ray background. Understanding, accurately characterizing, and reducing the absolute level of this X-ray background are fundamental to the X-ray analysis of faint X-ray sources and deep surveys.

The X-ray background can be classified into two major components: the cosmic X-ray background (CXB) and particle-induced non-X-ray background (NXB). The CXB is dominated by three main components: the Galactic local foreground, solar wind charge exchange emission, and unresolved X-ray emission by distant celestial sources. At lower energies (<1 keV) the dominant component is thermal emission from the Galactic Halo contributing at intermediate and high Galactic latitudes (Burrows & Mendenhall 1991; Snowden et al. 1991; War-

wick 2002; Lumb et al. 2002) and the Local Hot Bubble, a region of hot plasma ( $T \sim 10^6$  K) mostly filling the local cavity extending 100 pc away from the Sun (Snowden et al. 1998). Another component, which is composed of C VI, O VII, O VIII, Ne IX, and Mg XI line emission at lower energies ( $< 1$  keV), is the solar wind charge exchange produced when highly charged solar wind ions interact with neutral atoms in the solar system (Robertson & Cravens 2003; Koutroumpa et al. 2006). Unresolved X-ray emission from distant astrophysical sources, e.g., Active Galactic Nuclei (AGNs), contributes a power-law continuum spectrum that dominates at higher energies ( $>1$  keV) with a possible change in slope at lower energies and has been extensively studied in the literature, e.g., Lumb et al. (2002); Moretti et al. (2009). The magnitude of this component varies with position on the sky and it clearly suffers from cosmic variance (Hickox & Markevitch 2007). If an observation is deep enough to resolve the brightest sources (e.g., the strong shot noise), the residual contribution reaches to the expected cosmic variance given the  $\text{Log } N - \text{log } S$  relation (see for example Fig. 9 in (Moretti et al. 2009) and discussion therein).

The non X-ray background due to particles in missions operating above the Earth’s magnetic belts consists of two major background components: soft protons focused by the mirrors onto the focal plane and particle-induced instrumental background. Soft protons that are generated in the Solar corona and in the Earth’s magnetosphere with energies less than a few 100 keV can follow the optical path through the telescope and be focused onto the detectors. The spectral shape of this component can be described by a power-law continuum with highly variable magnitude and slope (Kuntz & Snowden 2008). When present, soft protons can increase the total background intensity by three orders of magnitude on short timescales of  $10-10^4$  s (Kuntz & Snowden 2008). They deposit most of their energy near the surface of the detector and produce valid event patterns (Gastaldello et al. 2017).

On the other hand, the unfocused particle-induced internal detector background is generated by energetic Galactic Cosmic Ray (GCR) primaries with energies from several tens of MeV to several GeV. GCR particles consisting of protons, electrons, and He ions are subject to variations over the Solar cycle. These incoming particles interact with the detector and produce secondary particles. The interactions constitute the major components of the unfocused portion of the particle-induced instrumental background (Kuntz & Snowden 2008; Snowden et al. 2008; von Kienlin et al. 2018). Based on their high total energies or the pattern of pixels excited in the event, particle events generated by primary GCRs are mostly discarded on board by the event processing (e.g., by the Minimum Ionizing Particle, MIP, rejection algorithm for *XMM-Newton*) to prevent them from saturating the limited bandwidth for telemetry (Lumb et al.

2002). However, the secondary electrons and photons due to this unfocused component deposit charge in the detector that it is challenging to distinguish from X-ray events from celestial sources and thus contribute significantly to (and often dominate) the quiescent instrumental background.

Quantifying the particle-induced instrumental background of X-ray observatories is not a trivial process and needs careful examination of observations while the detector is not exposed to sky. The *XMM-Newton* observatory, carrying two types of silicon-based X-ray detectors on board, the European Photon Imaging Camera (EPIC) MOS (Turner et al. 2001) and the EPIC pn (Strüder et al. 2001), provides an excellent opportunity to explore the instrumental background of silicon-based X-ray detectors. The unexposed corners of the *XMM-Newton* EPIC MOS detector that are masked off and the MOS data obtained when the filter wheel is in the closed position (FWC data) serve as estimators of the particle background for each observation that are used in the X-ray analysis of faint extended sources (De Luca & Molendi 2004; Kuntz & Snowden 2008; Gastaldello et al. 2017). The particle background of *XMM-Newton* EPIC-pn is difficult to predict and eliminate due to the fact that the unexposed region on the detector is small, i.e., statistics on the background level is limited.

In this paper, we examine the long-term variability of the unfocused EPIC-pn background. We present results from an analysis of all archival EPIC-pn data in the small window mode (SWM) with the filter wheel closed and MIP rejection disabled. The filter wheel closed observations with 1.05 mm of Al shielding do not allow any photons from celestial sources or soft protons to reach the focal plane. Additionally, all of the pixel data from both valid events and normally rejected particle tracks (GCR primaries) are telemetered to the ground in SWM mode observations. This set-up provides a unique opportunity to quantitatively investigate the relationship between the energetic primaries (i.e., GCRs) and the secondaries that mimic X-rays from celestial sources which constitute the dominant component of the instrumental background. We describe our sample and data analysis methods in Section 2. Our results for the *XMM-Newton* EPIC-pn SWM observations are described in Section 3. Our conclusions are given in Section 4.

This work was originally performed as part of a program to develop algorithms for improved background characterization and reduction for the *Athena* Wide-Field Imager (WFI) Science Products Module (SPM) (Burrows 2018; Bulbul et al. 2018; Grant 2018). One of the goals of the SPM would have been to use the full data stream from the WFI, not just the ground science event data available to the observer, to reduce the instrumental background. In an effort to better understand the instrumental background in X-ray observatories, we examined the *XMM-Newton* EPIC-pn SWM data as described in this paper and modeled the WFI background

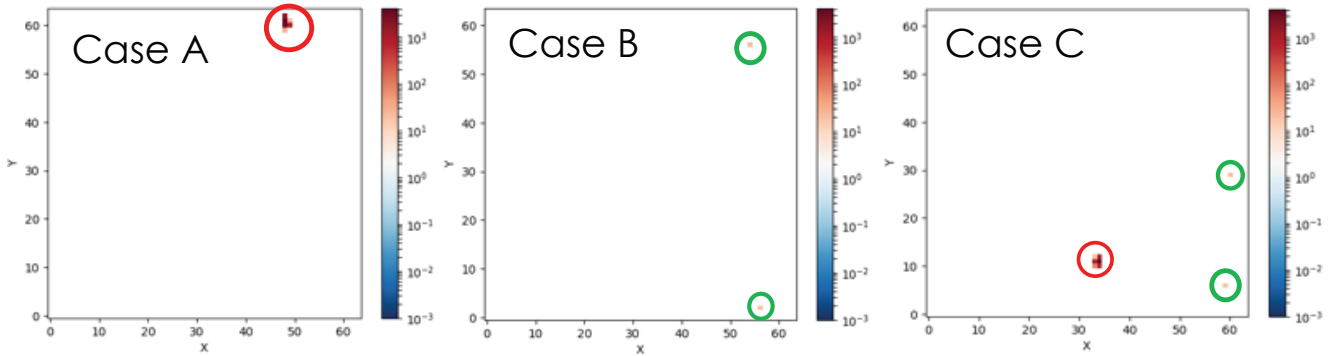


**Figure 1.** Frames with just particle tracks (Case A), valid events (Case B), and both particle tracks and valid events (Case C) are shown. The circles in red mark the detected primary particle events, while the green circles show the secondary valid events.

using the GEANT4 software (Tenzer et al. 2010). The latter modeling was done using the measured particle background at the *Athena* orbit (L2) with a mass model of the flight instrument (von Kienlin et al. 2018). Results from this study will be presented in a separate publication (Miller et al. 2019).

## 2. XMM-NEWTON EPIC-PN DATA ANALYSIS

### 2.1. Filter-Wheel Closed Slew and Pointed Observations

The EPIC-pn CCD camera is one of the primary instruments on on-board *XMM-Newton*, with a collecting area of  $\sim 2500 \text{ cm}^2$  at 1 keV and a 27.2 arcmin by 26.2 arcmin field of view over the broad energy range of 0.1 keV to 12 keV (Strüder et al. 2001). The *XMM-Newton* EPIC-pn data used in this work were taken during slews when the filter wheel was closed and performed in the SWM. In this mode, a 63 pixel by 64 pixel (4.3 arcmin by 4.4 arcmin) region on detector CCD4 is active and the read-out time is 5.67 ms, roughly a factor of 13 faster than the full-frame readout time of the primary science observing mode (full frame mode). A total of 309 observations have been completed since 2007 between revolutions 1360–3217, with typical exposures of 3–7 ks, adding up to a total exposure time of 1 Ms. The observation IDs and exposure times of the slew FWC observations are given in Table 4.

FWC observations are performed with 1.05 mm aluminum shielding, preventing low-energy soft protons and X-rays from celestial sources from reaching the EPIC-pn detector. Thus, FWC exposures contain only the particle-induced internal detector background, generated as a result of interactions of energetic Galactic Cosmic Rays ( $E > 100 \text{ MeV}$ ) with the material surrounding the EPIC-pn camera. Additionally, in the observations taken in the SWM set-up, the standard minimum ionizing particle (MIP) rejection algorithm, which identifies and automatically eliminates the pixels above a certain energy threshold and invalid patterns identified on board from the telemetered data, is inactive. As a

result, these observations represent an ideal data set to characterize the long term behavior of the *XMM-Newton* EPIC-pn internal background, since the ground observer has full access to *all* pixels above a threshold set by the ground observer. The data consist of electronic readout noise (at lowest energies, hot pixels, columns, and read-out noise), primary high energy GCRs, secondaries generated by high energy galactic cosmic rays, and particle-induced X-rays (continuum and fluorescent lines, von Kienlin et al. 2018).

The SWM frame time is sufficiently short in a sufficiently small readout area that the particle rate is much smaller than the frame rate. We thus have the unique opportunity to associate the normally rejected charged-particle events with the valid events that comprise the instrumental background. Since these observations are mostly dominated by the unfocused X-ray background, we use the term non-X-ray background (NXB) for these FWC slew observations hereafter.

For a comparison, we also examine the pointed *XMM-Newton* EPIC-pn SWM observations from two celestial sources: observations of the AB Doradus star system with the closed and thick filters, and a supernova remnant G21.5–0.9 (SNR 21.5–09, hereafter) performed with the thin filter. The details of these observations are given in Table 5. The AB Doradus observations with the closed filter are not expected to include any source photons (NXB dominated), while the observation with the thick filter is expected to be dominated by soft protons. A detailed analysis of the comparison between these two observations with different set-up will be explored in another article (Bulbul et al., in prep). SNR 21.5–09 observations, on the other hand, are dominated by photons from the supernova remnant in the FOV in the 2–7 keV band, while the contribution from the non X-ray background is subdominant. These pointed observations, taken in the SWM set-up, are similarly telemetered to the ground with the “on-board” MIP rejection algorithm inactive, thus including all pixels above the energy threshold. Having a longer uninterrupted expo-

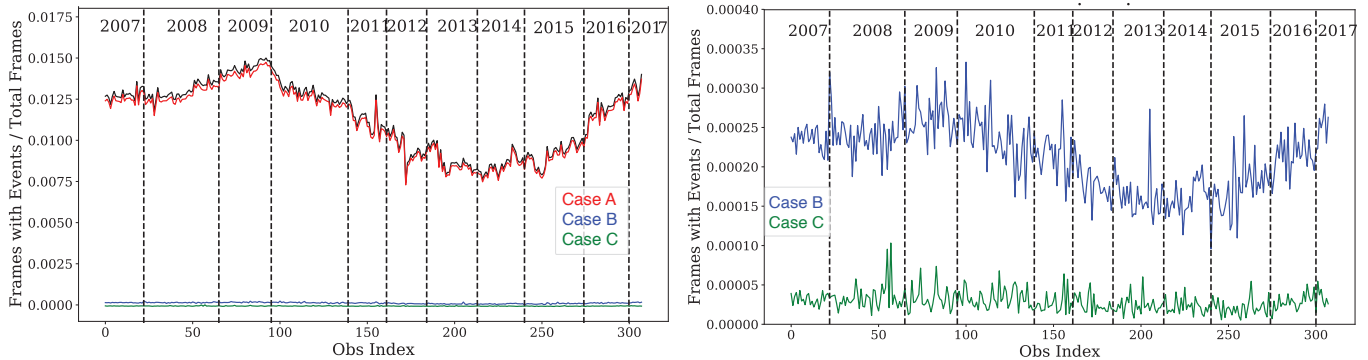


**Figure 2.** Left: The fraction of frames with just primary particle events (red; Case A), just secondary valid events (blue; Case B), and with both valid and particle events (green; Case C) as a function of time. Curve in black shows the total rate of particle events. Strong modulation with the Solar cycle observed for all the frames indicates that the *XMM-Newton* EPIC-pn unfocused background is dominated by Galactic cosmic rays. Right: Zoom onto Case B and Case C frame to enhance the visibility of the Solar modulation cycle.

sure time, these data provide information on short term variability of the unfocused X-ray background.

## 2.2. Data Reduction and Analysis

We first run the standard the Science Analysis Software *SAS* algorithm *epchain* to eliminate hot pixels and columns from the data and to form event lists for single exposures and for a given list of CCDs from the relevant observation data files (ODF) (Gabriel et al. 2004). We note that a non-standard parameter setting is selected in the *epchain* runs to switch off the “on-ground” MIP rejection. We then construct individual frames from the event files using the frame rate of 5.67 ms. The total number of frames constructed is given in Table 4. We examined a total of  $\sim 1.86 \times 10^8$  frames in the *XMM-Newton* EPIC-pn slew observations in this work. These observations span 10 years covering a full solar cycle.

After the construction of frames, we run an image segmentation algorithm on each frame to identify the independent event islands. This algorithm finds connected pixels and traces the long charge tracks of the energetic particle interactions. The charge of each event island is determined by the total charge enclosed in that particular event island. The centroids of these event islands are defined by the maximally charged pixel. We then assign a pattern ID by the pattern detection algorithm, i.e., *epchain*, to each event island. We note that this image segmentation algorithm developed by our team, is not the same algorithm used by the on board software.

The standard *XMM-Newton* EPIC-pn event processing flags event islands with pattern ID  $\leq 12$  as valid events, while particle events are marked with pattern IDs  $> 12$ <sup>1</sup>. The pattern ID is related to the number and pattern of the CCD pixels triggered for an X-ray

event above a certain threshold. The pattern IDs with 0 mark valid single pixel events, double pixel events are marked with pattern IDs 1–4, while triple and quadruple events have pattern IDs of 5–8 and 8–12, respectively. We note that in this FWC data set, the valid events are dominated by secondary particles that are produced by interactions of primary GCRs with the surroundings of the instrument. This component is mostly composed of secondary electrons and photons that deposit their energy in the active volume of the detector. The contributing secondary electrons are generated in ionization processes, while the secondary photons are mainly generated in bremsstrahlung and inelastic scattering processes (see von Kienlin et al. 2018 for more detail). In this work, we only consider valid events in the 2–7 keV energy band to avoid low-energy detector noise, unless otherwise noted. The event islands marked with pattern IDs  $> 12$  are mostly the incoming background GCR particles ( $\sim 200$  MeV–GeV), and Supra-Thermal Ions (STIs), mostly protons, accelerated in the Heliosphere to energies up to  $< 100$  keV hitting the detector (von Kienlin et al. 2018). These particle event islands are identified based on their patterns and the total charge encapsulated within the island. For most of these energetic events, there exists more than one pixel with a total charge exceeding the saturation level of the analog-to-digital converter (ADC; corresponding to 22.5 keV when MIP rejection is off). In those cases, the centroid of a particle event island is the maximally charged pixel last read by the image segmentation algorithm.

## 2.3. Classification of Frames

We next analyze the data sets on a frame-by-frame basis and identify event islands and divide the frames into four categories: frames with just particle tracks (Case A), frames with only valid events (Case B), frames with at least one particle track and at least one valid event (Case C), and frames with no particle tracks or

<sup>1</sup> [https://xmm-tools.cosmos.esa.int/external/xmm\\_user\\_support/documentation/uhb/epic\\_evgrades.html](https://xmm-tools.cosmos.esa.int/external/xmm_user_support/documentation/uhb/epic_evgrades.html)

**Table 1.** Fractions of Frames

Frame Type	Number of Frames	% Fractions
Case A	2089948	1.12
Case B	39186	0.02
Case C	5175	0.003
Case D	184541368	98.8

events (Case D). This categorization allow us to examine the frames with particle primaries without a secondary (Case A), secondaries that are created by particle primaries but not detected on the same frame (Case B), and the frames with the primary particle events and their secondaries detected on the same frame (Case C). Figure 1 illustrates the subdivision of frames. We find that overall the total number of Case A frames is 2089948, while 39186 of the frames are in the Case B, and 5175 of the frames are in Case C categories.

### 3. RESULTS

In the next subsections, we investigate the spectral properties, light curves, and spatial correlations between valid events and particle tracks in Case A, B, and C frames in detail.

#### 3.1. Long Term Variability

Investigating the temporal changes in the number of frames, we find that the overwhelming majority of the frames are empty and fall under the Case D category independent of solar cycle or orbit (see Figure 2). We find that overall the total number of Case A frames is 2089948 (1.12% of the total), while 39186 (0.02%) of the frames are Case B, 5175 (0.003%) of the frames are Case C, and the remainder (98.8%) are empty Case D frames (see 1). The temporal changes in the fractional A, B, and C frame rates are shown in Figure 2. The clear modulation with solar cycle observed in the fraction of Case A, B, and C frames is consistent with the previously observed modulations in the count rates in unexposed corners of MOS2 detector, EPIC Radiation Monitor on board of *XMM-Newton* (Gastaldello et al. 2017), and *Chandra* high energy (12–15 keV) count rate for the ACIS-S3 CCD as a function of year.<sup>2</sup> GCR flux is modulated in anti-correlation with solar activity due to the solar wind (Neher & Anderson 1962). While, Tthe Earth’s magnetic field provides a varying degree of geomagnetic shielding from these GCR particles, the level of the modulation depends on the energy of GCRs. The observed modulation on the EPIC-pn data shows that the FWC data are dominated by GCRs.

#### 3.2. Branching Ratios of Valid Events

Having the largest number of valid events, Case B frames dominate the unfocused background of the *XMM-Newton* EPIC-pn. We next examine the branching ratios, i.e., the fraction of the patterns of the valid events (singles, doubles, triples, and quadruples) in Case B frames, where only secondary events are detected. We detect a total number of 39190 valid events in non X-ray background observations (i.e., slew filter-wheel-closed observations listed in Table 4). The fractions of these valid patterns in Case B frames are shown in Table 2. Of the total valid events,  $65.6 \pm 0.2\%$  of them are singles,  $31.3 \pm 0.2\%$  are doubles, while  $1.47 \pm 0.06\%$  and  $1.59 \pm 0.06\%$  are triples and quadruples, respectively. Comparing these ratios with Case B frames observed in the closed filter AB Doradus observations, of the total 4172 valid events,  $65.3 \pm 0.7\%$  are singles,  $32.1 \pm 0.7\%$  are doubles, and triples and quadruples make up  $1.0 \pm 0.1\%$  and  $1.6 \pm 0.2\%$  of them, respectively. These pattern fractions are consistent with the ratios observed in the NXB slew observations, indicating that the 2–7 keV energy band of the AB Doradus observations with the filter closed is also dominated by the unfocused background of the *XMM-Newton* EPIC-pn. Case B frames for the SNR 21.5–09 observations include a total of 170114 valid events and have a lower fraction of singles ( $61.6 \pm 0.1\%$ ) and a larger percentage of doubles ( $34.5 \pm 0.1\%$ ) is detected compared to the AB Doradus and NXB observations.

In Case C frames of the NXB observations, we find a total of 3622 valid events in the 2–7 keV band. The majority of the valid events ( $67.8 \pm 0.8\%$ ) are singles, while doubles make up  $30.1 \pm 0.7\%$  of the total events. We find that  $1.0 \pm 0.2\%$  and  $1.1 \pm 0.2\%$  are triples and quadruples, respectively. Fractions of the valid patterns in Case C frames are shown in Table 2. Examining AB Doradus observations with the closed filter, we find a much lower number of valid events (a total of 322) in the Case C frames compared to Case B frames, consistent with the results we find in NXB observations (see Figure 2). Of these events  $69.4 \pm 2.6\%$  are singles,  $28.5 \pm 2.5\%$  are doubles,  $1.0 \pm 0.6\%$  and  $1.0 \pm 0.6\%$  of them are triples and quadruples. The branching ratios in this band are consistent with the fractions of valid event patterns observed in the slew NXB SWM data, indicating that the 2–7 keV band of AB Doradus observations is dominated by the EPIC-pn’s unfocused X-ray background, as in the Case C frames.

In Case C frames in the SNR 21.9-05 observations (a total of 4663 frames), the fraction of singles is lower ( $60.7 \pm 0.7\%$ ), while doubles are higher ( $35.9 \pm 0.7\%$ ) compared to both NXB dominated slew and AB Doradus observations in the source dominated hard band. Sparse statistics of triples and quadruples do not allow us to compare their branching ratios to the unfocused X-ray background. The key result here is that the valid events that make up the instrumental background have slightly different branching ratios to celestial X-rays in

<sup>2</sup> <http://space.mit.edu/cgrant/cti/cti120/bkg.pdf>

**Table 2.** Pattern Distribution of valid events in Case B and Case C frames of the Non-Xray Background (NXB) taken in filter-wheel closed set up, AB Doradus observations in filter-wheel closed set up, and SNR 21.5–09 observations performed with thin filter.

Frames	NXB		AB Doradus		SNR 21.5–09	
	Closed Flt.		Closed Flt.		Thin Flt.	
	Case B	Case C	Case B	Case C	Case B	Case C
Singles	$65.6 \pm 0.2$	$67.8 \pm 0.8$	$65.3 \pm 0.7$	$69.4 \pm 2.6$	$61.6 \pm 0.1$	$60.7 \pm 0.7$
Doubles	$31.3 \pm 0.2$	$30.1 \pm 0.7$	$32.1 \pm 0.7$	$28.5 \pm 2.5$	$34.5 \pm 0.1$	$35.9 \pm 0.7$
Triples	$1.47 \pm 0.06$	$1.0 \pm 0.2$	$1.0 \pm 0.1$	$1.0 \pm 0.6$	$2.0 \pm 0.6$	$1.7 \pm 0.2$
Quadruples	$1.59 \pm 0.06$	$1.1 \pm 0.2$	$1.6 \pm 0.2$	$1.0 \pm 0.6$	$1.9 \pm 0.6$	$1.6 \pm 0.2$

the 2-7 keV band. High energy events with harder spectrum have more probability to have high split event ratios compared to the low energy photons with soft spectrum. Since SNR 21.9-05 has a harder spectrum, the split event ratios are expected to be higher than the split event ratios in the non X-ray background.

### 3.3. Time Interval Between Valid Events

We further investigate whether there is a temporal correlation between the arrival times of valid events. The distribution of the arrival times of successive events in Case B frames in the 2–7 keV energy band is shown in Figure 3. If the valid events are independent of each other, the distribution is expected to be exponential, with a time constant close to the mean time between events (the reciprocal of the mean rate of Case B frames). We find that the mean difference in the arrival times of the valid events in Case B frames is 26.7 second, which is comparable to the time constant of the exponential distribution. There is no evidence of a characteristic time interval between events shorter than the mean time interval. This also confirms that the 2–7 keV band is dominated by the unfocused background and that our filtering has removed most of the instrumental artifacts associated with the long reset time constant of the output amplifiers (Freyberg et al. 2004). We do not find any significant departures from expectations in the arrival time of valid events depending on the particle environment.

### 3.4. Spectral Properties of Valid and Particle Events

We first extract spectra of all valid events based on their patterns in Case B frames (see Figure 4). Overall the spectra of singles and doubles are quite flat, while the spectra of triples and doubles are slightly positively sloped towards higher energies. Additionally, we removed events that are located at the detector boundaries since it is challenging to determine if the event detected at the boundary is a single pixel event or is the partially collected charge of an event that landed off the active area of the detector.

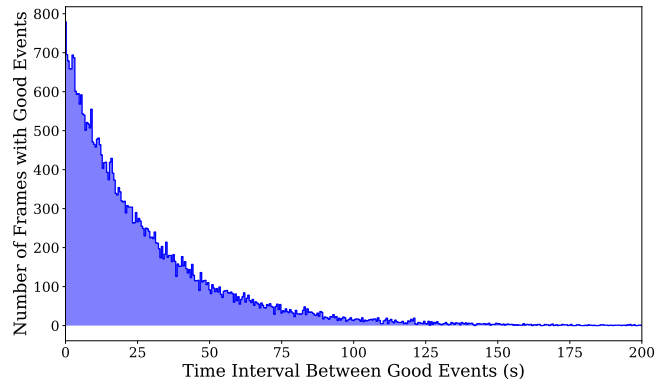


**Figure 3.** Distribution of the time intervals between valid events in Case B frames showing the exponential form expected for uncorrelated events. The exponential time constant is equal to the mean time between Case B events.

Next, we investigate the spectral properties of the particle tracks in Case A and C frames. The total energy of particle tracks is obtained by summing the charge in spatially connected pixels found by our image segmentation algorithm. We then generate the spectra of these particle events and normalize them by the total frames in each observation (as given in Table 4). The spectra of the particle events are shown in Figure 5. The overwhelming statistical power in Case A frames (see Figure 2) allows us to examine particle spectra in different phases of the solar cycle: the observations in the solar activity plateau between 2007–2008 (in magenta), 2012–2015 (in cyan), decline in solar activity between 2008–2010 (in orange) and 2015–2017 (dark blue), and increase in solar activity between 2010–2012 (in green). We then overplot the spectra of particle events in Case C frames from all epochs (2007–2017) in red in Figure 5 with the same bin size of 7 keV. Due to the limited number of Case C frames, we combine all particle events detected between 2007 and 2017. Figure 5 shows spectra of particle events in Case A and Case C frames (left) and the difference between them (right). The spectra of the particle events in Case A frames are strikingly sim-

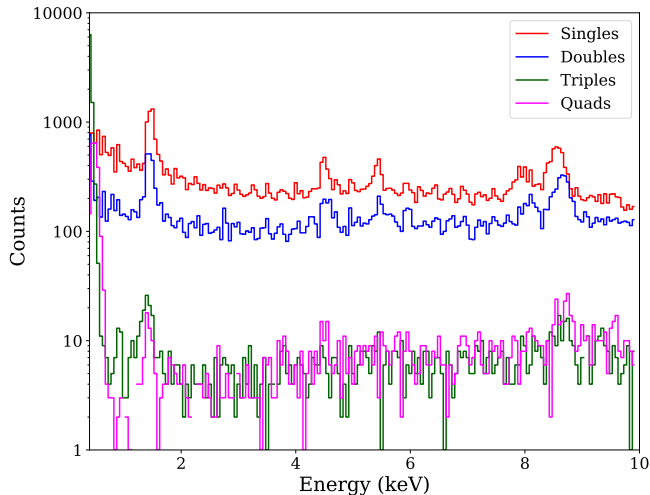


**Figure 4.** Pulse-height spectra of valid events (single pixel events in red, doubles in blue, triples in green, and quadruples in purple) in Case B frames observed in the *XMM-Newton* EPIC-pn filter-wheel-closed observations. Fluorescent instrumental lines of Si  $K\alpha$  (1.75 keV), Ti  $K\alpha$  (4.5 keV), Cr  $K\alpha$  (5.4 keV), Cu  $K\alpha$  (8.0 keV), and Zn  $K\alpha$  (8.6 keV) are visible in the spectra.

ilar to one another and independent of the solar cycle. We find a significant difference between the spectra of particle events that are detected in Case C frames and those detected in Case A frames. We observe a steeper slope in the energy band  $< 200$  keV in the Case A spectra, and above  $> 200$  keV the Case C spectrum flattens. This may indicate that the particle events that create showers of valid events while passing through the detector housing (in Case C frames) originate from a different particle population or geometry than primary particles detected in Case A frames. The observed flattening of the spectrum of Case C frames above 1.5 MeV is likely due to combination of limited statistics, lack of sensitivity, and ADC saturation limit.

Another implication of Figure 5 is that if the spectra of particle events in the Case B and Case C frames are normalized to the counts in the 250-750 keV energy band, the spectral slopes become consistent between these two spectra. In this case, an excess of low energy particle events is observed on the Case C frames compared to the Case B frames in the lower energy band below 200 keV. This may indicate that low energy particle events are more likely to convert into showers and create secondaries that are detected on the detector.

### 3.5. Spatial Correlation Between Particle and Valid Events

We further examine the distribution of distances between the centroid position of the valid and particle events in Case C frames. In both cases, the centroids

of the events are determined by the maximally charged pixels. In the case of the particle event islands, when highly energetic particles interact with the detector, often more than one pixel gets charged at the ADC saturation limits, i.e., 22.5 keV with MIP rejection off. In these cases, the center of the event is marked as the last saturated pixel in an event island to be read. The distribution of distance between particle events and their secondary valid events for the slew NXB observations is shown in blue in Figure 6. The form of the distribution expected for uncorrelated events in these frames is plotted as a dashed yellow curve. The significant excess of event pairs at small separations indicates that the valid events in the immediate  $< 30$  pixel area around the particle events are highly spatially correlated with the associated particle track. We note that, due to the small active area of the detector in the SWM observations (63 pixel  $\times$  64 pixel), our analysis is not sensitive to correlations at large scales.

As a next step, we divide the valid events based on their patterns and reexamine the spatial correlations of singles, doubles, triples, and quadruples. We find a similar correlation between these patterns and particle events independent of their patterns. We also looked for energy dependence in the correlation between particle tracks and related events by dividing particle events into categories: particles with low-energies,  $< 200$  keV, and high energy particles with  $> 200$  keV (see Section 3.4). We do not observe any differences in the spatial correlation between valid events and particle tracks as a function of energy of the particle events.

Next, we examine the spatial correlation between valid/particle event pairs observed in Case C frames for the pointed observations through the closed filter of the AB Doradus star system (black distribution in Figure 6). As expected, this histogram is similar to the one for the slew NXB observations (e.g., there is a significant excess at small spatial scales up to 30 pixels) indicating that the 2–7 keV band is dominated by the unfocused X-ray background.

The shape of the spatial correlation between valid events and particle tracks for the SNR 21.5-0.9 data (cyan in Figure 6) is similar to the form expected for uncorrelated events (yellow curve). However, the distribution of separations is more peaked than expected for pairs of randomly distributed events. This is because, although a particle is equally likely to land anywhere on the detector, the supernova is centered on the chip, causing the distribution of source photons to be peaked there. This indicates that the 2–7 keV energy band for the SNR 21.5–09 observations is dominated by photons from the supernova remnant and the unfocused X-ray background is subdominant.

These results are the basis of the self-anti-coincidence (SAC) method, used to reduce secondary events associated with a particle primary. This method of partial vetoing of valid events around particle tracks shows

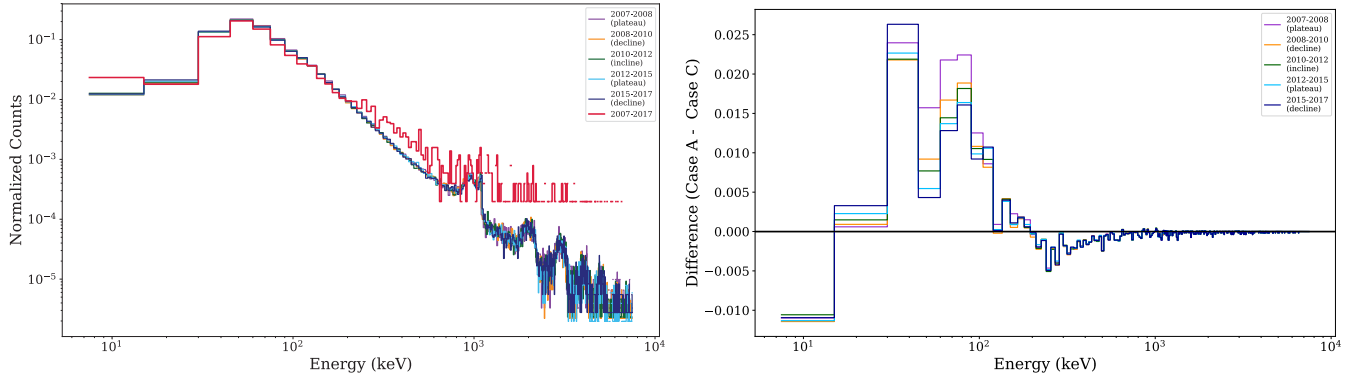


**Figure 5.** Left Panel: Pulse-height spectra of the particle events in Case A frames. The data have been divided into five time intervals to sample the variation of the particle spectra with the Solar cycle and normalized by the number of frames in each period. Over-plotted in red is the pulse-height spectrum of the particle events in Case C frames between 2007 and 2017. The periodic structure observed at high energies is an aliasing effect due to binning and ADC saturation limit. Flattening of the spectrum of the red (Case C) histogram above  $\sim 200$  keV relative to the other histograms (Case A) is clearly visible. Right Panel shows the difference between the normalized pulse height spectra of Case A frames and Case C frames.

promise at reducing the systematic error produced by the instrumental background at the expense of eliminating events from real source X-rays (based on private communication with Silvano Molendi). We find that by eliminating events that fall within 30 pixels of the peak of a particle track, the particle-induced background of the *XMM-Newton* EPIC-pn can be reduced by  $\sim 10\%$  (see Figure 7). The results summarized here from the *XMM-Newton* EPIC-pn FWC observations can be used to reduce the particle background level of the future silicon-based X-ray detectors. For instance, the earlier EPIC MOS results were used to optimize FWC rotation strategy to sample particle background component during *Athena* WFI observations of faint objects (Gastaldello et al. 2017; von Kienlin et al. 2018).

### 3.6. Short Term Variability of the Particle Environment

Owing to the long term coverage of the *XMM-Newton* EPIC-pn slew observations with the filter-wheel closed between years 2007 and 2017, we are able to probe short term variability of particle events in Case A frames. We examine the light curves of particle events in Case A frames in five epochs defined by the phase of the solar cycle as shown in Figure 2 (plateau in 2007, solar minimum in 2009, increase in solar activity in 2011, solar maximum in 2014, decrease in solar activity in 2016). The variability of the rate of particle events in Case A frames in 10 observations taken close together in time, with 100 s binning, is shown in Figure 8 for each epoch. We note that the observations used in producing light curves in this section differ from the observations used to generate the spectra in Section 3.4. The mean, standard deviation, and skewness of the light curve counts of these particle events are given in Table 3. The dashed curves indicate a normal distribution with Poisson standard de-

viation. There is no statistically significant variability of the particle tracks in any epoch.

We find that the mean values of the particle counts vary between 133 and 276, depending on the solar activity (see Table 3); however, the standard deviations (12-19) are remarkably small and independent of solar cycle. The mean of particle event counts observed per 100 s can be as high as 276 during solar minimum, while it can be as low as 133 during solar maximum. In general, each distribution is well-matched to the Poisson distribution expected for a constant mean rate (shown in dashed curves). We do not observe significant irregularities or outlier particle events in the light curves.

Similarly, we examine the light curves of particle events in Case A frames of the pointed *XMM-Newton* EPIC-pn SWM observations of AB Doradus and SNR 21.5–09. The histograms of the light curves are similarly tightly distributed around the mean as observed in NXB observations, close to the expected Poisson distribution. The AB Doradus observations were taken in 2002 and 2004, and the observed mean values are 133 and 179 while the Sun was active. The AB Doradus observations with thick filter were taken in 2017, when the solar activity was approaching its minimum, therefore a mean rate of 239 particle tracks is observed during those observations. These count rates are consistent with the count rates we observe in NXB dominated slew observations. The SNR 21.5–09 observations were also taken in 2017 while solar activity was approaching minimum. The observed mean value of 239 indicates that these observations were performed when the solar activity was at minimum.

To further test the similarities in the background light curves against the Poisson distribution, we computed Kolmogorov-Smirnov statistics. The Kolmogorov-Smirnov test determines the probability of two sam-



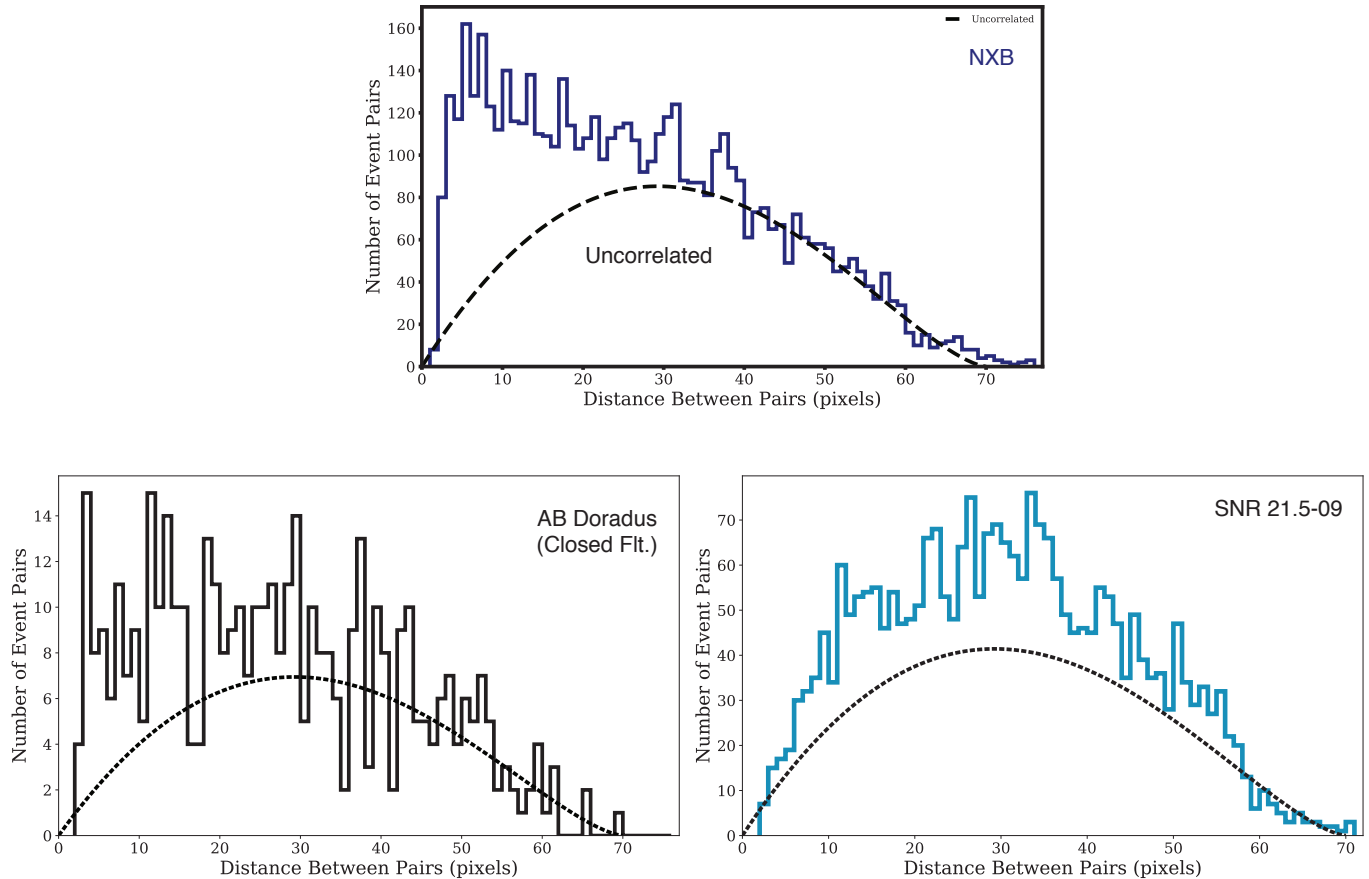


**Figure 6.** The distribution of distances between valid events in the 2–7 keV energy band and the particle events detected in Case C frames of the NXB with closed filter (in blue), SNR 21.5–09 with thin filter (in black), and AB Doradus with closed filter (in cyan). The dashed curve in yellow indicates the expected distribution for uncorrelated event pairs. Valid events in the immediate  $\sim 30$  pixel vicinity of the particle events in NXB and AB Doradus observations are highly correlated, indicating that the 2–7 keV band of these observations are dominated by the unfocused background of *XMM-Newton* EPIC-pn. Although statistics of Case C frames are limited, an evidence of spatial correlation in small spatial scales ( $<30$  pixels) is visible in the AB Doradus observations on the right panel. The two-point correlation function in the SNR 21.5–09 observations shows a distribution consistent with the theoretical distribution of uncorrelated events, indicating that 2–7 keV band is dominated by the emission from the supernova remnant.

ples being drawn from the same distribution. The high values of probabilities ( $> 0.73$ ) indicate that these background light curves distributions are originating from the same underlying Poisson distribution.

We also show distributions of the number of valid events in the 2–7 keV energy band in Case B frames in Figure 9, binned for longer time intervals (200 s) to allow for the lower event rate. Similarly, we do not observe any significant deviations from Poisson distributions for the numbers of particle related events in the filter-wheel closed data.

#### 4. CONCLUSIONS

In this work, we present analysis of the unfocused X-ray background of the *XMM-Newton* EPIC-pn operating

in small window mode with a fast frame time. These observations were taken while *XMM-Newton* was slewing to a variable source that was to be observed in SWM, while the filter-wheel was in the closed position and the MIP rejection algorithm was turned off. This dataset uniquely allows us to study temporal, spectral, and spatial properties of particle primaries and their secondaries generated as a result of the interactions with the detector housing, which constitute the unfocused instrumental background for the science observer. We also compare our results from the unfocused background, NXB, with the pointed filter closed observations of a star system AB Doradus and observations of a supernova remnant SN 21.5–09 taken with the thin filter. Owing to the

**Table 3.** Statistics of Light Curves of Particle Event Rates in Case A Frames binned for 100s

Date	Epoch	Mean	Std Dev.	Skewnes	KS test	D-value	p-value
2007	Plateau	238	16	0.01	0.16	0.76	
2009	Solar Mimumum	276	19	0.23	0.13	0.93	
2011	Solar Activity Increase	210	18	0.06	0.10	0.99	
2014	Solar Maximum	159	14	0.24	0.13	0.93	
2016	Solar Activity Decrease	230	18	-0.01	0.13	0.93	
2002	AB Doradus (Closed Flt.)	133	12	0.08	0.17	0.76	
2004	AB Doradus (Closed Flt.)	179	15	-0.82	0.25	0.78	
2017	AB Doradus (Thick Flt.)	239	15	0.25	0.13	0.94	
2017	SNR 21.5–09 (Thin Flt.)	239	16	0.05	0.16	0.76	

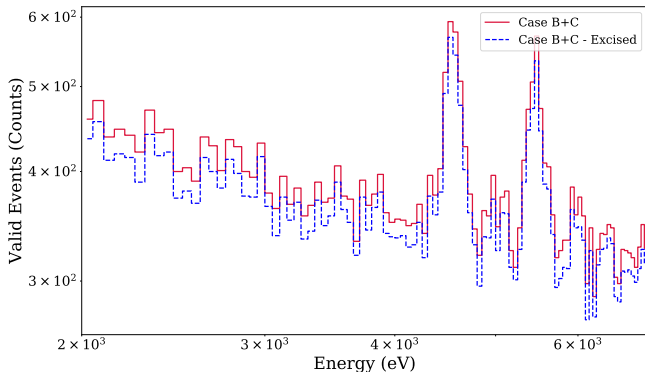


**Figure 7.** Pulse-height spectrum of valid events detected in Case B and C frames (in red). Rejecting valid events associated with a primary GCR by using SAC with a 30 pixels exclusion radius would reduce the particle-induced background level of the *XMM-Newton* EPIC-pn by  $\sim 10\%$  in the 2–7 keV energy band. The resulting background spectrum is shown in dashed blue.

large number of frames, we were able to independently study the frames with just primary particles (Case A), with just secondary valid events (Case B), and with both primary particle and secondary valid events (Case C). Our major results are as follows.

- Examining the branching ratios of event morphologies, we find that the vast majority of valid events in Case B frames of NXB observations are single pixel events ( $65.6 \pm 0.2\%$ ) and double pixel events ( $31.3 \pm 0.2\%$ ). Comparing these ratios with the observations of a supernova remnant, we find that in both cases, Case B frames have a significantly smaller fraction of singles ( $61.6 \pm 0.1$ ), and larger fraction of doubles ( $34.5 \pm 0.1\%$ ). The fraction of singles in Case C frames of the unfocused NXB ( $67.8 \pm 0.8\%$ ) is also higher compared to that

in the supernova observations ( $60.7 \pm 0.7\%$ ). In both cases, the differences are statistically significant. That is, the valid events in the instrumental background have somewhat different branching ratios than those of the celestial X-rays.

- The mean difference between the observed arrival times of successive valid events in Case B frames matches the reciprocal of the event rate, as expected. We do not observe any structure in the distribution of the time intervals suggestive of a temporal correlation between background events, or detector or background effects on the time interval between valid events. As expected, all background events appear to be independent and uncorrelated.
- The energy spectrum of the particle tracks in frames with valid events is somewhat flatter than that of the tracks in frames with no valid events. This result indicates that the particle events detected with secondary events in the same frame (Case C) might be due to a different population of particles passing through, or a different geometry compared to the primary particle events that do not generate secondary showers in the detector housing. We also found that when the spectra of particle events are normalised to the high energy band (250–750 keV), an excess of low energy particle are observed in the Case C frames (frames with at least one primary and secondary particles) compared to the Case B frames (frames with just primaries). This may indicate that low energy particles are more likely to interact with the detector housing and create secondary particle showers.
- We find a significant spatial correlation between particle and valid events in Case C frames on small spatial scales up to 30 pixels (4500 microns) of

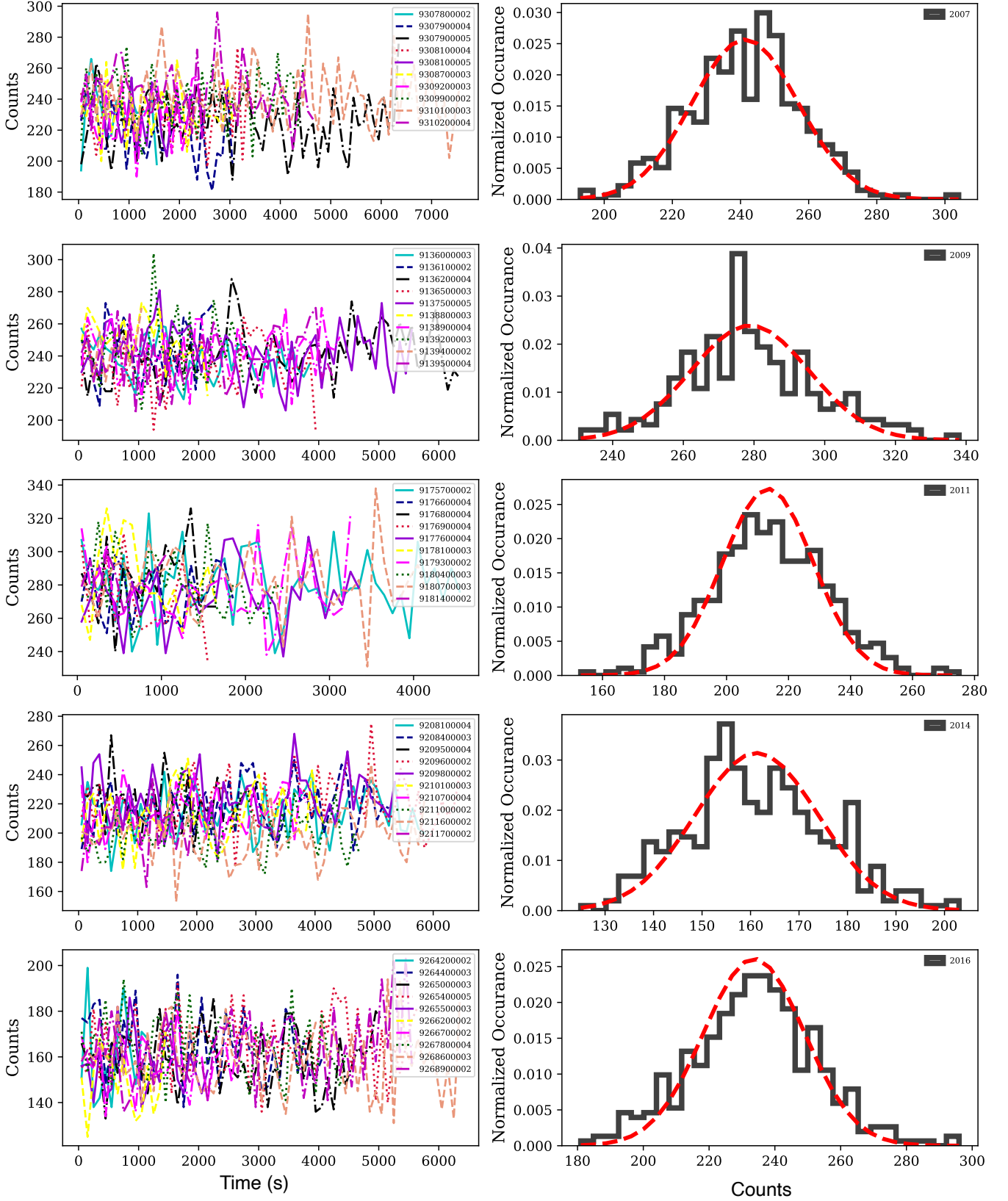


**Figure 8.** The light curves of particle events detected in Case A frames per 100 s binning for five different epochs in the solar cycle are shown on the left panels. The dashed lines in the right hand panels show the expected Poisson distributions around the mean. The distributions of count rates of particle events in these observations in each epoch are shown on the right panels.

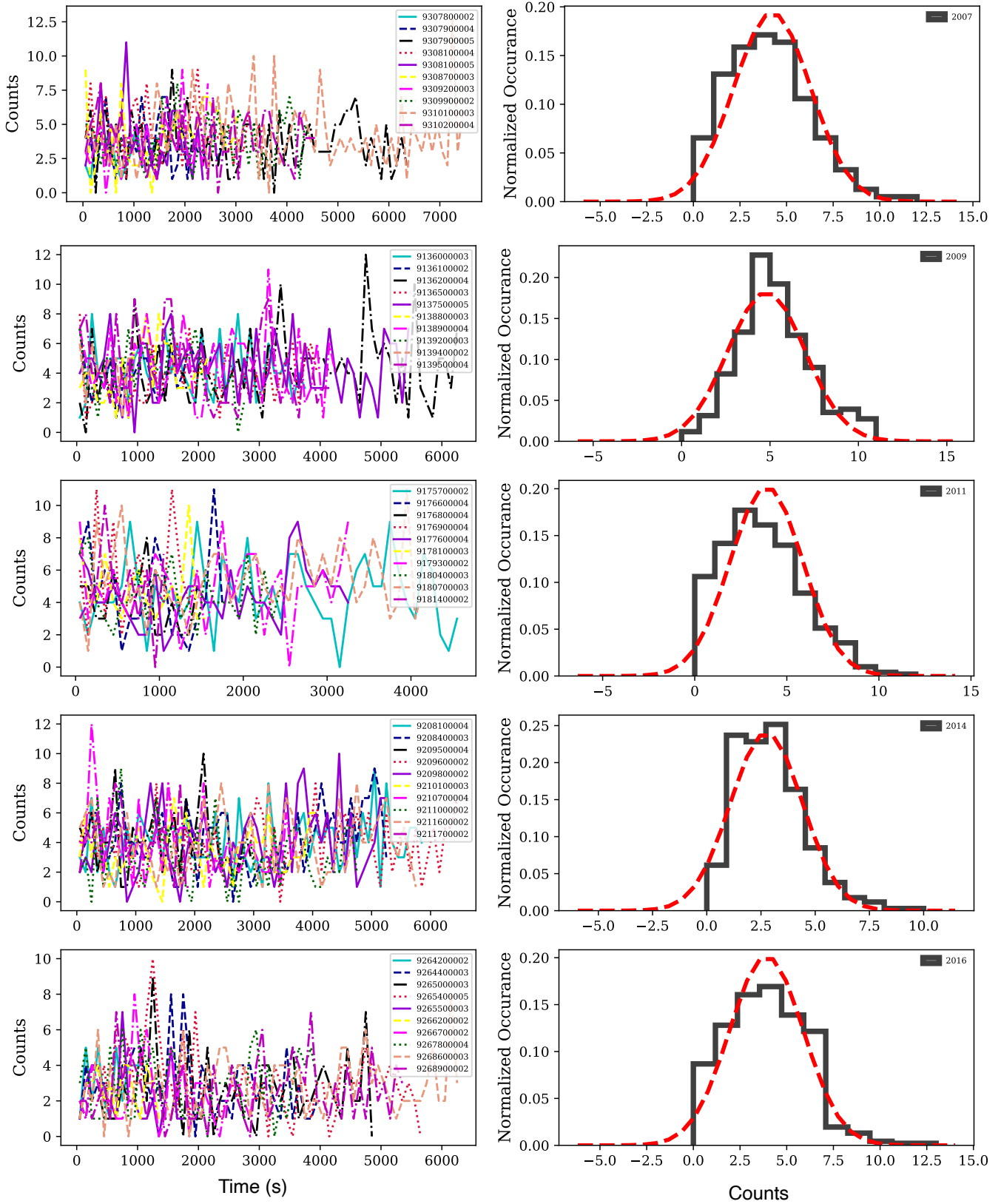


**Figure 9.** The light curves of valid events in 2 to 7 keV band detected in Case B frames per 200s binning for five different epochs in the solar cycle are shown on the left panels. The dashed lines in the right hand panels show the expected Poisson distributions around the mean. The distributions of count rates of particle events in these observations in each epoch are shown on the right panels.

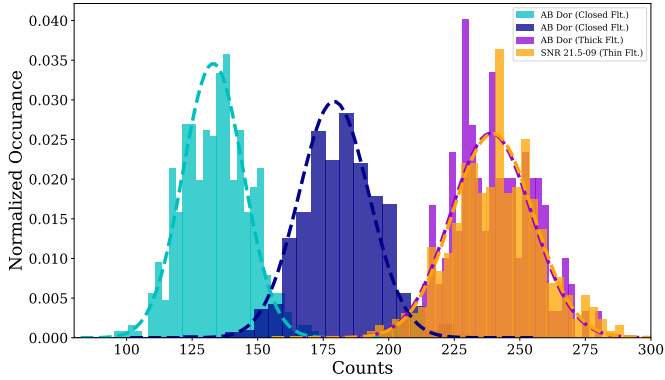


**Figure 10.** Distribution of particle event counts per 100 s bin obtained from light curves of the pointed observations of the AB Doradus star system taken in two different filter configurations; filter closed and with the thick filter. The observations were taken in 2002, 2004, and 2017. Comparing mean count rates with the count rates observed in NXB data (see Table 3), we can infer that the filter closed observations were taken during solar maximum, while the 2017 observations were performed during solar minimum. The unfocused background level measured in the FWC data and solar activity are closely correlated.

the unfocused background observations with the closed filter in the 2–7 keV band. In the observations of the supernova remnant SNR 21.5–09 no spatial correlation between the valid events and particle events is observed, as expected. Rejecting valid events (“self-anticoincidence” or “SAC”) within 30 pixels around the primary GCRs reduces the absolute level of the particle-induced background of *XMM-Newton* EPIC-pn by  $\sim 10\%$  in the 2–7 keV energy band.

- Light curves of particle events in Case A frames display a tight distribution, with mean particle counts of 133 to 276 per 100 s bin, depending on the phase of the solar cycle. The mean number of particle events per 100 s bin can be as high as 276 during solar minimum, while it can be as low as 133 during solar maximum. The sample standard deviations of the count per 100 s bin are consistent with expectations for Poisson distributions with the observed means. There is no evidence for any short-term temporal variability in the GCR component of the instrumental background, beyond what is expected for Poisson noise. KS-test results indeed indicate that the distribution of count rates in the light curves of Case A and Case B frames are consistent with the Poissonian distribution around the mean rate. These means and distributions can be used to monitor particle rates and estimate the level of unfocused background of future X-ray imaging detectors.

- Light curves of valid events (secondaries generated by primary GCRs) also display a tight distribution around the mean, consistent with the expected Poissonian distribution. Similarly, there is no significant evidence for any short-term temporal variability in the secondary background events. These observed rates closely correlate with the solar cycle and particle rates and can be used to predict the level of unfocused X-ray background.

Similar analyses of the unfocused component of the X-ray detector background have been performed on the *Chandra* stowed ACIS data and the Neil Gehrels Swift Telescope XRT data (e.g., Bartalucci et al. 2014; Grant 2018; Bulbul et al. 2018). Results we present in this work should help to understand and reduce the particle background level in other Si-based X-ray detectors (e.g., the Wide Field Imager on *Athena* and the *eROSITA* instrument on board the Spectrum Roentgen Gamma observatory). The SWM frame time of 5.67 ms is similar to the *Athena* WFI default frame, allowing us to validate GEANT4 simulations of the *Athena* WFI unfocused background (see Miller et al. 2019).

Beyond validating the GEANT4 simulations for the *Athena* WFI, this study also lays the ground work for application of self-anticoincidence to reduce the unfocused background in silicon-based X-ray detectors, e.g. WFI on board of *Athena* (Nandra et al. 2013), *eROSITA* on board of SRG (Merloni et al. 2012), EPIC on board of *XMM-Newton* (Jansen et al. 2001), and HDXI on board of *Lynx* (Gaskin et al. 2019). The results obtained from this work will be used to develop both on-board and ground-based algorithms to better characterize and improve background rejection for silicon-based X-ray imaging detectors. The self-anticoincidence method, and the results presented in this work, will help reduce the *Athena* WFI particle background and increase the signal-to-noise in background-dominated observations, such as galaxy cluster outskirts and deep surveys, enhancing the science return of *Athena*.

## ACKNOWLEDGEMENTS

Authors thank the anonymous referee for helpful comments on the draft. We gratefully acknowledge support from NASA grant NNX17AB07G, administered by Penn State, and from NASA contracts NAS 8-37716 and NAS 8-38252.

This paper made use of the simulations from GEANT software (Tenzer et al. 2010) and *XMM-Newton* SAS analysis software (Gabriel et al. 2004). This work made use of SciPy (Jones et al. 2001), matplotlib, a Python library for publication quality graphics (Hunter 2007), Astropy, a community-developed core Python package for Astronomy (Astropy Collaboration et al. 2013), NumPy (Van Der Walt et al. 2011).

APPENDIX  
A. OBSERVATIONS

**Table 4.** *XMM-Newton* EPIC-pn Small Window Mode Observations Taken in the Filter-Wheel Closed Set-up during slewing phase.

Obs. Index	Obs. ID	Revolution	Exposure (ks)	Number of Frames	Obs. Index	Obs. ID	Revolution	Exposure (ks)	Number of Frames
0	9136000003	1360	3.91	690114	155	9213400002	2134	3.4	599994
1	9136100002	1361	2.37	418658	156	9214900004	2149	1.42	249893
2	9136200004	1362	6.42	1132080	157	9217500002	2175	1.85	326346
3	9136500003	1365	4.07	717519	158	9218200004	2182	2.58	454189
4	9137500005	1375	5.65	995629	159	9218300002	2183	2.47	435767
5	9138800003	1388	2.24	395752	160	9219200004	2192	3.13	551326
6	9138900004	1389	4.42	778932	161	9223300002	2233	5.31	935852
7	9139200003	1392	2.86	504355	162	9223700003	2237	2.7	475590
8	9139400002	1394	1.15	201914	163	9225900003	2259	3.18	560297
9	9139500004	1395	4.31	759510	164	9226100002	2261	5.88	1035931
10	9139700002	1397	2.18	383899	165	9226400004	2264	2.63	464485
11	9140100004	1401	1.37	241883	166	9227500006	2275	3.48	614237
12	9141000003	1410	4.08	719023	167	9227600002	2276	2.24	394874
13	9142800004	1428	5.71	1005950	168	9229000002	2290	1.84	324827
14	9143300002	1433	3.71	654472	169	9229600003	2296	1.84	323646
15	9144300004	1443	6.17	1087659	170	9229700003	2297	1.52	267659
16	9144500003	1445	2.97	522981	171	9229900003	2299	1.51	265961
17	9144700003	1447	0.99	175325	172	9230900003	2309	4.29	756196
18	9144900005	1449	1.33	234024	173	9231800002	2318	3.82	673051
19	9145700003	1457	5.2	917470	174	9232100004	2321	6.81	1199982
20	9146300006	1463	3.33	587072	175	9233000003	2330	2.29	403991
21	9147500002	1475	1.88	331127	176	9233200003	2332	3.94	693939
22	9147900002	1479	1.86	327992	177	9233900005	2339	4.44	782505
23	9148000004	1480	1.28	225991	178	9236300002	2363	3.8	669151
24	9148400003	1484	2.5	440018	179	9236600002	2366	5.91	1042100
25	9149500002	1495	4.75	838019	180	9236700002	2367	6.49	1144493
26	9151000002	1510	6.67	1175239	181	9236900002	2369	4.91	865822
27	9151000003	1510	3.59	632906	182	9238200002	2382	5.89	1038778
28	9151300002	1513	5.52	973663	183	9238700004	2387	4.35	766698
29	9151600004	1516	1.98	349686	184	9239400003	2394	3.85	678823
30	9151700002	1517	0.95	168322	185	9240900002	2409	3.38	595051
31	9152300002	1523	2.14	377646	186	9241200002	2412	2.11	371796
32	9152400002	1524	3.32	585622	187	9241500002	2415	5.36	944903
33	9152700003	1527	3.79	667745	188	9241600002	2416	1.11	196163
34	9152900002	1529	3.54	624743	189	9242200003	2422	2.04	359330
35	9153000003	1530	4.17	735806	190	9242700002	2427	2.28	401729
36	9153100004	1531	5.72	1007747	191	9243000003	2430	3.56	628516
37	9153200003	1532	5.31	936525	192	9245700004	2457	2.3	405332

*Table 4 continued*

Table 4 (continued)

Obs. Index	Obs. ID	Revolution	Exposure (ks)	Number of Frames	Obs. Index	Obs. ID	Revolution	Exposure (ks)	Number of Frames
38	9153300002	1533	4.7	827869	193	9247900002	2479	1.03	182172
39	9153400002	1534	3.7	652071	194	9248700002	2487	1.23	216006
40	9153400004	1534	4.92	868326	195	9248900002	2489	2.41	425183
41	9153600002	1536	5.47	964802	196	9248900003	2489	3.63	640579
42	9153600003	1536	6.18	1090252	197	9249100002	2491	6.75	1189397
43	9153900002	1539	1.05	184286	198	9249300002	2493	6.28	1106857
44	9154200004	1542	6.26	1103389	199	9249400002	2494	3.42	603517
45	9154300003	1543	2.9	510531	200	9249500003	2495	6.09	1073205
46	9154400005	1544	3.06	538903	201	9249600002	2496	3.48	614271
47	9154600005	1546	4.39	773231	202	9249700002	2497	3.49	615429
48	9156800003	1568	5.83	1027723	203	9249800002	2498	1.72	302452
49	9158100002	1581	4.66	822194	204	9249900002	2499	4.02	708999
50	9158900004	1589	3.34	589018	205	9252900006	2529	0.98	171979
51	9160000002	1600	3.28	578523	206	9253300003	2533	3.06	540308
52	9160700004	1607	1.44	253915	207	9254400002	2544	1.25	220908
53	9160800004	1608	5.82	1025948	208	9254500004	2545	4.1	723228
54	9160900002	1609	2.95	519505	209	9254600004	2546	4.71	830219
55	9161000002	1610	0.95	167732	210	9256500002	2565	5.84	1028961
56	9161300002	1613	1.08	189574	211	9256600002	2566	4.34	764502
57	9161500004	1615	2.03	358285	212	9257300002	2573	1.56	274811
58	9161600002	1616	6.03	1062547	213	9258700002	2587	4.26	751265
59	9161900002	1619	1.53	268946	214	9258800002	2588	3.16	557816
60	9162100003	1621	3.5	617167	215	9259300002	2593	5.78	1018257
61	9163100002	1631	1.93	341051	216	9261200003	2612	5.39	950948
62	9164900002	1649	2.56	450613	217	9261800002	2618	5.7	1004257
63	9164900003	1649	3.04	536480	218	9262500003	2625	5.94	1046693
64	9165500004	1655	2.32	408867	219	9263300002	2633	1.54	271100
65	9166200003	1662	0.99	175344	220	9264200002	2642	1.24	219011
66	9168100003	1681	1.48	260533	221	9264400003	2644	4.18	737026
67	9169500002	1695	1.39	245523	222	9265000003	2650	5.15	908458
68	9169600003	1696	1.55	273414	223	9265400005	2654	5.74	1012829
69	9169700004	1697	3.36	591780	224	9265500003	2655	2.25	396033
70	9169800002	1698	4.11	725288	225	9266200002	2662	1.57	276761
71	9169900004	1699	4.56	804166	226	9266700002	2667	3.01	531492
72	9170200002	1702	2.06	362767	227	9267800004	2678	4.55	801427
73	9170300002	1703	4.63	816310	228	9268600003	2686	6.46	1139449
74	9170500003	1705	3.97	700703	229	9268900002	2689	5.64	993993
75	9171000002	1710	5.26	926909	230	9269100003	2691	1.24	219322
76	9171000003	1710	2.56	450836	231	9269300002	2693	4.37	769649
77	9171100004	1711	1.28	225877	232	9270200002	2702	2.88	508607
78	9171600003	1716	4.29	756501	233	9272100002	2721	6.61	1165708
79	9172300002	1723	4.09	720996	234	9272200003	2722	3.91	689470
80	9175700002	1757	4.69	826810	235	9272300003	2723	1.79	316186
81	9176600004	1766	1.97	346701	236	9272400004	2724	6.2	1093794
82	9176800004	1768	1.7	300522	237	9273200003	2732	4.78	842060
83	9176900004	1769	1.62	285310	238	9273400004	2734	6.58	1160738
84	9177600004	1776	3.42	603085	239	9274300003	2743	5.68	1002279

Table 4 continued

Table 4 (continued)

Obs. Index	Obs. ID	Revolution	Exposure (ks)	Number of Frames	Obs. Index	Obs. ID	Revolution	Exposure (ks)	Number of Frames
85	9178100003	1781	1.75	309354	240	9276100002	2761	0.95	167169
86	9179300002	1793	3.36	591642	241	9276400002	2764	2.79	492081
87	9180400003	1804	2.58	454489	242	9276600002	2766	3.79	668182
88	9180700003	1807	4.22	744111	243	9276600003	2766	3.47	611061
89	9181400002	1814	1.19	209206	244	9276700003	2767	4.7	828186
90	9181700003	1817	2.36	415451	245	9278000004	2780	3.44	607388
91	9181900003	1819	4.2	740381	246	9278900002	2789	3.99	703211
92	9182100003	1821	5.27	928537	247	9279400003	2794	0.94	166137
93	9182200003	1822	4.81	848729	248	9280600003	2806	1.98	349925
94	9182500003	1825	3.03	534405	249	9281000002	2810	3.13	552697
95	9185700003	1857	1.52	267126	250	9281200003	2812	3.62	637549
96	9187200003	1872	2.3	405573	251	9281300003	2813	2.18	384111
97	9187300003	1873	3.35	591401	252	9285000003	2850	5.78	1018841
98	9187400002	1874	4.27	751985	253	9285400002	2854	1	176060
99	9187400003	1874	2.52	443917	254	9285400003	2854	3.17	559730
100	9188300003	1883	1.09	192227	255	9285600002	2856	0.98	173367
101	9189000003	1890	2.53	446735	256	9285700003	2857	3.8	669560
102	9189200004	1892	3.79	668616	257	9288200003	2882	1.08	191254
103	9190100002	1901	5.01	882669	258	9289500004	2895	1.73	305505
104	9190400003	1904	1.39	244955	259	9289800002	2898	1.13	200067
105	9190600003	1906	2.32	409140	260	9290800002	2908	3.45	608332
106	9191000002	1910	6.44	1134925	261	9291100003	2911	3	529685
107	9191100005	1911	3.12	549656	262	9291500002	2915	1.03	181709
108	9191300004	1913	4.98	877200	263	9291600004	2916	3.01	530927
109	9191600003	1916	2.83	498338	264	9291800002	2918	4.92	867689
110	9191700004	1917	5.73	1010187	265	9291900002	2919	2.67	470591
111	9191800002	1918	5.73	1010697	266	9292200002	2922	5.23	921950
112	9192100003	1921	2.25	397558	267	9292300002	2923	3.36	592678
113	9193100002	1931	2.14	377032	268	9292300003	2923	3.32	585432
114	9193200002	1932	3.09	545221	269	9292400005	2924	3.6	635465
115	9194500007	1945	2.16	380834	270	9293100002	2931	6.35	1118778
116	9194800004	1948	3.55	625570	271	9293400002	2934	1.11	196290
117	9195000003	1950	3.73	658118	272	9293500002	2935	1.21	213551
118	9196600002	1966	5.18	913961	273	9293700002	2937	4.79	844386
119	9196900002	1969	1.25	220960	274	9294700014	2947	1.85	325342
120	9197000002	1970	5.27	929152	275	9294800004	2948	1.6	282729
121	9197500003	1975	2.27	399390	276	9294900005	2949	4.03	710343
122	9198100002	1981	2.22	390596	277	9305600003	3056	4.35	767630
123	9198300002	1983	4.06	716621	278	9305600004	3056	4.58	807780
124	9198400003	1984	2.51	443394	279	9305700003	3057	5.35	943508
125	9198700006	1987	1.09	192494	280	9305700005	3057	2	352481
126	9198900002	1989	1.82	320276	281	9305800002	3058	4.78	843571
127	9198900004	1989	4.43	780710	282	9306300003	3063	2.3	405608
128	9199200004	1992	1.05	185637	283	9306400004	3064	6.67	1176203
129	9199500004	1995	1.91	336064	284	9307500002	3075	2.49	438811
130	9200100005	2001	3.19	563143	285	9307800002	3078	1.62	285357
131	9200200002	2002	3.23	568866	286	9307900004	3079	3.1	546744

Table 4 continued



**Table 4** (*continued*)

Obs. Index	Obs. ID	Revolution	Exposure (ks)	Number of Frames	Obs. Index	Obs. ID	Revolution	Exposure (ks)	Number of Frames
132	9200400003	2004	2.12	373047	287	9307900005	3079	6.48	1142453
133	9200800004	2008	4.74	835613	288	9308100004	3081	3.64	641870
134	9200900003	2009	1.74	307235	289	9308100005	3081	2.51	442592
135	9201300003	2013	4.14	730250	290	9308700003	3087	3.16	557727
136	9201400003	2014	1.66	292367	291	9309200003	3092	2.53	446555
137	9201500003	2015	6.49	1144810	292	9309900002	3099	4.56	804260
138	9202100003	2021	1.87	330235	293	9310100003	3101	7.66	1349994
139	9202900002	2029	4.21	741632	294	9310200004	3102	4.71	830686
140	9204700002	2047	1.6	282537	295	9311100002	3111	1.56	274181
141	9205700003	2057	6.36	1121529	296	9311100005	3111	5.01	883409
142	9207100003	2071	2.63	463072	297	9312000002	3120	0.97	170493
143	9207600004	2076	1.7	299695	298	9312000003	3120	3.08	542823
144	9207700003	2077	3.48	612781	299	9312000004	3120	2.03	358103
145	9208100004	2081	5.96	1051690	300	9313500002	3135	4.54	800551
146	9208400003	2084	5.35	942755	301	9313900002	3139	2.8	492855
147	9209500004	2095	3.19	561571	302	9315100002	3151	1.52	267559
148	9209600002	2096	6.56	1156232	303	9316200002	3162	4.86	857242
149	9209800002	2098	5.43	957569	304	9316200003	3162	1.55	273718
150	9210100003	2101	4.22	744294	305	9317200002	3172	1.54	271656
151	9210700004	2107	3.95	696954	306	9319100004	3191	4.31	760519
152	9211000002	2110	4.87	857875	307	9321200004	3212	3.71	654218
153	9211600002	2116	5.94	1047642	308	9321700003	3217	1.98	348438
154	9211700002	2117	2.14	376952					

**Table 5.** Pointed *XMM-Newton* EPIC-pn Small Window Mode Observations

Source	Obs. ID	Year	Filter Set up	Exp. ks	Number of Frames ( $\times 10^6$ )
AB Doradus	0134522101	2002	Closed Ft.	49	8.55
AB Doradus	0160362901	2004	Closed Ft.	56	9.87
AB Doradus	0791980401	2017	Thick Ft.	12	2.08
SNR 21.5–09	0804250201	2017	Thin Ft.	41	7.14

*Software:* **GEANT4** (Tenzer et al. 2010), *XMM-Newton SAS* (Gabriel et al. 2004), **Matplotlib** (Hunter 2007), **NumPy** (Van Der Walt et al. 2011), **Astropy** (Astropy Collaboration et al. 2013), **SciPy** (Jones et al. 2001).

## REFERENCES

- Astropy Collaboration, Robitaille, T. P., Tollerud, E. J., et al. 2013, *A&A*, 558, A33, doi: [10.1051/0004-6361/201322068](https://doi.org/10.1051/0004-6361/201322068)
- Bartalucci, I., Mazzotta, P., Bourdin, H., & Vikhlinin, A. 2014, *A&A*, 566, A25, doi: [10.1051/0004-6361/201423443](https://doi.org/10.1051/0004-6361/201423443)
- Bulbul, E., Kraft, R., Nulsen, P., et al. 2018, in Society of Photo-Optical Instrumentation Engineers (SPIE) Conference Series, Vol. 10699, Space Telescopes and Instrumentation 2018: Ultraviolet to Gamma Ray, 106994G
- Burrows, D. e. a. 2018, in Society of Photo-Optical Instrumentation Engineers (SPIE) Conference Series, Vol. 10699, Space Telescopes and Instrumentation 2018: Ultraviolet to Gamma Ray, 1069954

- Burrows, D. N., & Mendenhall, J. A. 1991, *Nature*, 351, 629, doi: [10.1038/351629a0](https://doi.org/10.1038/351629a0)
- De Luca, A., & Molendi, S. 2004, *A&A*, 419, 837, doi: [10.1051/0004-6361:20034421](https://doi.org/10.1051/0004-6361:20034421)
- Freyberg, M. J., Briel, U. G., Dennerl, K., et al. 2004, in *Proc. SPIE, Vol. 5165, X-Ray and Gamma-Ray Instrumentation for Astronomy XIII*, ed. K. A. Flanagan & O. H. W. Siegmund, 112–122
- Gabriel, C., Denby, M., Fyfe, D. J., et al. 2004, *Astronomical Society of the Pacific Conference Series*, Vol. 314, *The XMM-Newton SAS - Distributed Development and Maintenance of a Large Science Analysis System: A Critical Analysis*, ed. F. Ochsenbein, M. G. Allen, & D. Egret, 759
- Gaskin, J. A., Swartz, D. A., Vikhlinin, A., et al. 2019, *Journal of Astronomical Telescopes, Instruments, and Systems*, 5, 021001, doi: [10.1117/1.JATIS.5.2.021001](https://doi.org/10.1117/1.JATIS.5.2.021001)
- Gastaldello, F., Ghizzardi, S., Marelli, M., et al. 2017, *Experimental Astronomy*, 44, 321, doi: [10.1007/s10686-017-9549-y](https://doi.org/10.1007/s10686-017-9549-y)
- Grant, C. e. a. 2018, in *Society of Photo-Optical Instrumentation Engineers (SPIE) Conference Series*, Vol. 10699, *Space Telescopes and Instrumentation 2018: Ultraviolet to Gamma Ray*, 10699158
- Hickox, R. C., & Markevitch, M. 2007, *ApJL*, 661, L117, doi: [10.1086/519003](https://doi.org/10.1086/519003)
- Hunter, J. D. 2007, *Computing In Science & Engineering*, 9, 90
- Jansen, F., Lumb, D., Altieri, B., et al. 2001, *A&A*, 365, L1, doi: [10.1051/0004-6361:20000036](https://doi.org/10.1051/0004-6361:20000036)
- Jones, E., Oliphant, T., Peterson, P., et al. 2001, *SciPy: Open source scientific tools for Python*.  
<http://www.scipy.org/>
- Koutroumpa, D., Lallement, R., Kharchenko, V., et al. 2006, *A&A*, 460, 289, doi: [10.1051/0004-6361:20065250](https://doi.org/10.1051/0004-6361:20065250)
- Kuntz, K. D., & Snowden, S. L. 2008, *A&A*, 478, 575, doi: [10.1051/0004-6361:20077912](https://doi.org/10.1051/0004-6361:20077912)
- Lumb, D. H., Warwick, R. S., Page, M., & De Luca, A. 2002, *A&A*, 389, 93, doi: [10.1051/0004-6361:20020531](https://doi.org/10.1051/0004-6361:20020531)
- Merloni, A., Predehl, P., Becker, W., et al. 2012, *arXiv e-prints*, arXiv:1209.3114.  
<https://arxiv.org/abs/1209.3114>
- Miller, E. D., Grant, C. E., Bautz, M., et al. 2019, *JATIS*, in prep.
- Moretti, A., Pagani, C., Cusumano, G., et al. 2009, *A&A*, 493, 501, doi: [10.1051/0004-6361:200811197](https://doi.org/10.1051/0004-6361:200811197)
- Nandra, K., Barret, D., Barcons, X., et al. 2013, *arXiv e-prints*. <https://arxiv.org/abs/1306.2307>
- Neher, H. V., & Anderson, H. R. 1962, *J. Geophys. Res.*, 67, 1309, doi: [10.1029/JZ067i004p01309](https://doi.org/10.1029/JZ067i004p01309)
- Robertson, I. P., & Cravens, T. E. 2003, *Geophys. Res. Lett.*, 30, 1439, doi: [10.1029/2002GL016740](https://doi.org/10.1029/2002GL016740)
- Snowden, S. L., Egger, R., Finkbeiner, D. P., Freyberg, M. J., & Plucinsky, P. P. 1998, *ApJ*, 493, 715, doi: [10.1086/305135](https://doi.org/10.1086/305135)
- Snowden, S. L., Mebold, U., Hirth, W., Herbstmeier, U., & Schmitt, J. H. M. 1991, *Science*, 252, 1529, doi: [10.1126/science.252.5012.1529](https://doi.org/10.1126/science.252.5012.1529)
- Snowden, S. L., Mushotzky, R. F., Kuntz, K. D., & Davis, D. S. 2008, *A&A*, 478, 615, doi: [10.1051/0004-6361:20077930](https://doi.org/10.1051/0004-6361:20077930)
- Strüder, L., Briel, U., Dennerl, K., et al. 2001, *A&A*, 365, L18, doi: [10.1051/0004-6361:20000066](https://doi.org/10.1051/0004-6361:20000066)
- Tenzer, C., Warth, G., Kendziorra, E., & Santangelo, A. 2010, in *Proc. SPIE, Vol. 7742, High Energy, Optical, and Infrared Detectors for Astronomy IV*, 77420Y
- Turner, M. J. L., Abbey, A., Arnaud, M., et al. 2001, *A&A*, 365, L27, doi: [10.1051/0004-6361:20000087](https://doi.org/10.1051/0004-6361:20000087)
- Van Der Walt, S., Colbert, S. C., & Varoquaux, G. 2011, *Computing in Science & Engineering*, 13, 22
- von Kienlin, A., Eraerds, T., Bulbul, E., et al. 2018, in *Society of Photo-Optical Instrumentation Engineers (SPIE) Conference Series*, Vol. 10699, *Space Telescopes and Instrumentation 2018: Ultraviolet to Gamma Ray*, 106991I
- Warwick, R. S. 2002, *arXiv Astrophysics e-prints*